TU Delft

Delft University of Technology

Document Version
Final published version

Licence
Dutch Copyright Act (Article 25fa)

Citation (APA)
Liu, T., Lu, H., Li, G., Niu, W., Leeflang, R. A., Wu, T. S., Dugulan, A. I., Yi, X., Liu, C., & More Authors (2026). Unsaturated ZrO_x Sites Boost C–C Coupling for Selective CO_2 Hydrogenation to Olefins. *Journal of the American Chemical Society*, *148*(19), 19925-19935. https://doi.org/10.1021/jacs.6c02733

Important note
To cite this publication, please use the final published version (if applicable).
Please check the document version above.

Copyright
In case the licence states “Dutch Copyright Act (Article 25fa)”, this publication was made available Green Open Access via the TU Delft Institutional Repository pursuant to Dutch Copyright Act (Article 25fa, the Taverne amendment). This provision does not affect copyright ownership.
Unless copyright is transferred by contract or statute, it remains with the copyright holder.

Sharing and reuse
Other than for strictly personal use, it is not permitted to download, forward or distribute the text or part of it, without the consent of the author(s) and/or copyright holder(s), unless the work is under an open content license such as Creative Commons.

Takedown policy
Please contact us and provide details if you believe this document breaches copyrights.
We will remove access to the work immediately and investigate your claim.

This work is downloaded from Delft University of Technology.

JACS
JOURNAL OF THE AMERICAN CHEMICAL SOCIETY
pubs.acs.org/JACS
Article

Unsaturated ZrO_x Sites Boost C−C Coupling for Selective CO_2 Hydrogenation to Olefins

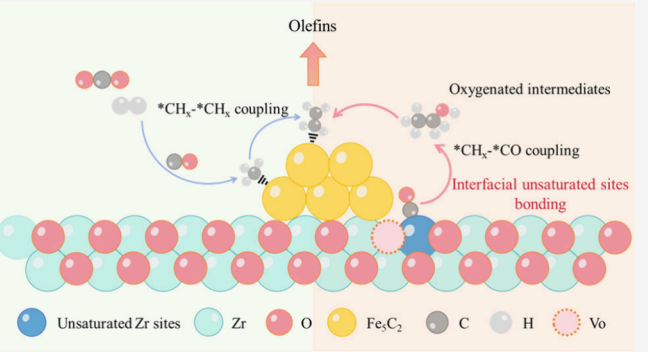
Tangkang Liu, Hanjun Lu, Guangchao Li,* Wentian Niu, Renzo A. Leeflang, Tai-Sing Wu, A. Iulian Dugulan, Xianfeng Yi, Chengyuan Liu, Long Zhao, Xinlin Hong,* Guoliang Liu,* Shik Chi Edman Tsang, and Anmin Zheng*

Cite This: J. Am. Chem. Soc. 2026, 148, 19925−19935

Read Online

ACCESS | Metrics & More | Article Recommendations | Supporting Information

ABSTRACT: Direct hydrogenation of CO_2 to synthetic fuels and olefins using renewable hydrogen remains challenging owing to the scarcity of low-cost, active, and highly selective catalysts. Current catalytic systems often exhibit either excessive CO selectivity or generate substantial alkanes to cause a low olefin-to-paraffin (O/P) ratio that limits hydrogen utilization efficiency. Herein, we report an unsaturated ZrO_x-modified iron catalyst (Na−Fe/*a*-ZrO_2) that delivers an olefin selectivity exceeding 80% among organic products, while suppressing the combined CO+CH_4 selectivity to below 25% and raising the O/P ratio to as high as ∼28. Multimodal *in situ/operando* spectroscopies and synchrotron-based vacuum ultraviolet photoionization mass spectrometry (SVUV-PIMS) demonstrate that unsaturated ZrO_x sites can modulate the activation modes of surface-bound *CO intermediates and selectively promote *CO insertion into alkyl species. This process consumes reactive intermediates that would otherwise desorb to form undesirable byproducts, thereby enabling selective olefin synthesis compatible with hydrogen-efficient CO_2 conversion.



INTRODUCTION

Against the backdrop of rising global olefin demand and limited oil resources, direct hydrogenation of CO_2 to olefins using green or blue hydrogen offers a promising route for converting greenhouse gases into synthetic fuels and olefins.[1−3] Despite its technological promise, techno-economic analysis indicates that hydrogen costs could account for over 50% of total production expenses in industry, constituting one of the key determinants of overall economic viability.[4,5] To establish a process with high hydrogen atom economy and sustainable carbon utilization, a key challenge lies in designing inexpensive and efficient catalysts that not only enhance CO_2/CO conversion but also suppress alkane (especially methane) production.[5−7] However, uncontrollable C−O bond activation and challenging C−C coupling present major obstacles to simultaneously optimizing hydrogen efficiency and carbon utilization in CO_2-to-olefins conversion, creating significant economic challenges to industrial-scale implementation. Thus, it is essential to develop stable catalytic systems capable of combining low alkane selectivity with high olefin yields.

Olefin synthesis from CO_2 hydrogenation can proceed via either CO_2-modified Fischer−Tropsch synthesis (CO_2−FTS) or a methanol-mediated coupling pathway (involving methanol synthesis plus methanol to hydrocarbons over oxide-zeolite bifunctional catalysts).[6,8,9] Compared to oxide-zeolite systems that often form substantial CO (selectivity for 30−50%) at relatively low CO_2 conversion, iron-based CO_2−FTS catalysts are widely employed for olefin production due to their high single-pass conversion, low cost, and natural abundance.[2,10−16] However, iron catalysts struggle to efficiently drive both C−O bond cleavage and C−C coupling because of the complex reaction kinetics in CO_2 hydrogenation.[3,6] A key limitation is their tendency to produce excessive methane and light alkanes, with typical selectivity ranging from 25% to 75% (excluding CO) and limited olefin-to-paraffin (O/P) ratio (typically 2−10), originating from their intrinsic promotion of CO_2/CO methanation.[17,18] To mitigate this issue, significant efforts have been devoted to modifying iron catalysts with amorphous oxide supports or promoters (e.g., alkali metals, Zn, Sr), which induce more synergistic sites that enhance C−C coupling via the carbide mechanism and tune hydrogenation activity, thereby lowering alkane selectivity to below 24%.[6,19−23] Moreover, Cu-modified iron catalysts have achieved alkane

Received: February 5, 2026
Revised: April 29, 2026
Accepted: April 30, 2026
Published: May 9, 2026



Downloaded via TU DELFT on June 4, 2026 at 15:13:39 (UTC).
See https://pubs.acs.org/sharingguidelines for options on how to legitimately share published articles.

ACS Publications
© 2026 American Chemical Society

https://doi.org/10.1021/jacs.6c02733
J. Am. Chem. Soc. 2026, 148, 19925−19935

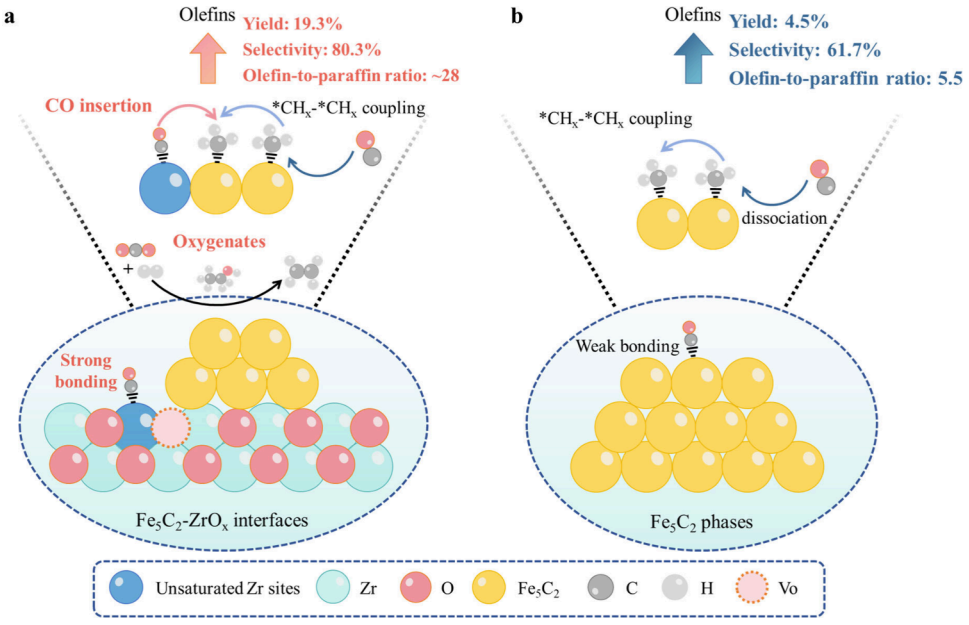


Figure 1. Direct hydrogenation of CO_2 to olefins over the Na−Fe/amorphous ZrO_2 and Na−Fe catalysts. Schematic illustration for the reaction paths occurring at the interfaces between unsaturated ZrO_x sites and Fe_5C_2 sites (a) and the sole Fe_5C_2 phases (b).

selectivity as low as 14.3%, though only under conditions where CO selectivity remains high (43.7%).[5] Thus, if desorbed CO could be utilized as monomeric units and coupled with surface-bound alkyl species to boost olefin synthesis, this strategy would not only decrease production costs but also maintain high carbon utilization. In light of the above, developing high-performing catalytic systems that simultaneously minimize C1 byproducts and maximize olefin yields with an ultrahigh O/P ratio under operating conditions remains a critical and unmet challenge.

Herein, we report that introducing unsaturated ZrO_x sites modulates the catalytic behaviors of Na−Fe catalysts for selective CO_2 hydrogenation to olefins, with a 4.3-fold yield relative to the unpromoted Na−Fe (Figure 1). Under optimized conditions (320 °C and 1 MPa), the Na−Fe/*a*-ZrO_2 achieves an unprecedented olefin selectivity of 80.3% at CO_2 conversion of 29.5%. More importantly, the selectivity toward valuable compounds (olefins + C_{2+} alcohols) reaches up to 89.6%, whereas the combined CH_4+CO selectivity is limited within 25%. The unsaturated ZrO_x species can regulate the activation modes of surface-bound *CO intermediates, thereby decreasing alkane selectivity to below 11% and remarkably increasing olefin-to-paraffin (O/P) ratio from 5.5 (on Zr-free Na−Fe catalyst) to ∼28. On the basis of *in situ* synchrotron-based vacuum ultraviolet photoionization mass spectrometry (SVUV-PIMS), multimodal *in situ/operando* spectroscopies, and chemisorption-pulse experiments, we reveal that the unsaturated ZrO_x sites predominantly facilitate the nondissociative activation of *CO and its subsequent insertion into alkyl species for C−C coupling, thereby driving olefin formation via C_{2+} oxygenated intermediates. Furthermore, this catalyst demonstrates high stability during a 160-h time-on-stream test, highlighting its promising potential for large-scale CO_2 utilization.

RESULTS AND DISCUSSION

Catalytic Performance in CO_2-Modified FTS to Olefins

As described in our previous work,[24] we synthesized amorphous ZrO_2 (*a*-ZrO_2, 505 m^2 g^{-1}) with abundant Zr-oxide nodes via a gel-assisted solvothermal method (see Supplementary Figure S1). This precursor is engineered to facilitate the formation of more unsaturated metal sites. Iron catalysts with varying Na and Fe content were then prepared on this support utilizing deposition-precipitation and impregnation methods. For comparison, a 2 wt % Na-modified Fe_2O_3, denoted as Na−Fe, was also prepared by the impregnation method. To further investigate the role of unsaturated metal sites in olefin synthesis, a small quantity of highly dispersed ZrO_x species (0.1−1 wt %) was introduced into the Na−Fe through the impregnation method. Detailed synthesis procedures and additional characterization data are available in the Supporting Information.

We began to evaluate the catalytic performance of catalysts for CO_2 hydrogenation to olefins at a H_2/CO_2 feed gas at 320 °C and 1 MPa. As shown in Figure 2a and Table S1, the unpromoted Na−Fe gives olefin selectivity (excluding CO) of 61.7% and high CO selectivity of 57.2% at a CO_2 conversion of 16.9% and an olefin-to-paraffin (O/P) ratio of 5.5. In contrast, utilizing *a*-ZrO_2 as the support significantly suppresses CO selectivity (decreases from 57.2% to 18.7%), and the selectivity for alkanes is as low as 10.4% with enhanced carbon chain growth capability (α = 0.67) (Figure 2b). Concurrently, both olefin selectivity and CO_2 conversion increase substantially. This highlights the critical role of ZrO_x species in promoting CO conversion and subsequent C−C coupling, as evidenced by enhanced activity of atomically dispersed ZrO_x-modified Na−Fe catalysts (Figures S2−S3 and Table S2). Optimization studies examining the effects of Na and Fe loading (Figures S4−S5) identified an optimal composition of 2 wt % Na and 20 wt % Fe, referred to herein as Na−Fe/*a*-ZrO_2 without further notice. Notably, this catalyst delivers olefin selectivity (excluding CO) of up to 80.3% and valuable C_{2+}OH selectivity

https://doi.org/10.1021/jacs.6c02733
J. Am. Chem. Soc. 2026, 148, 19925−19935

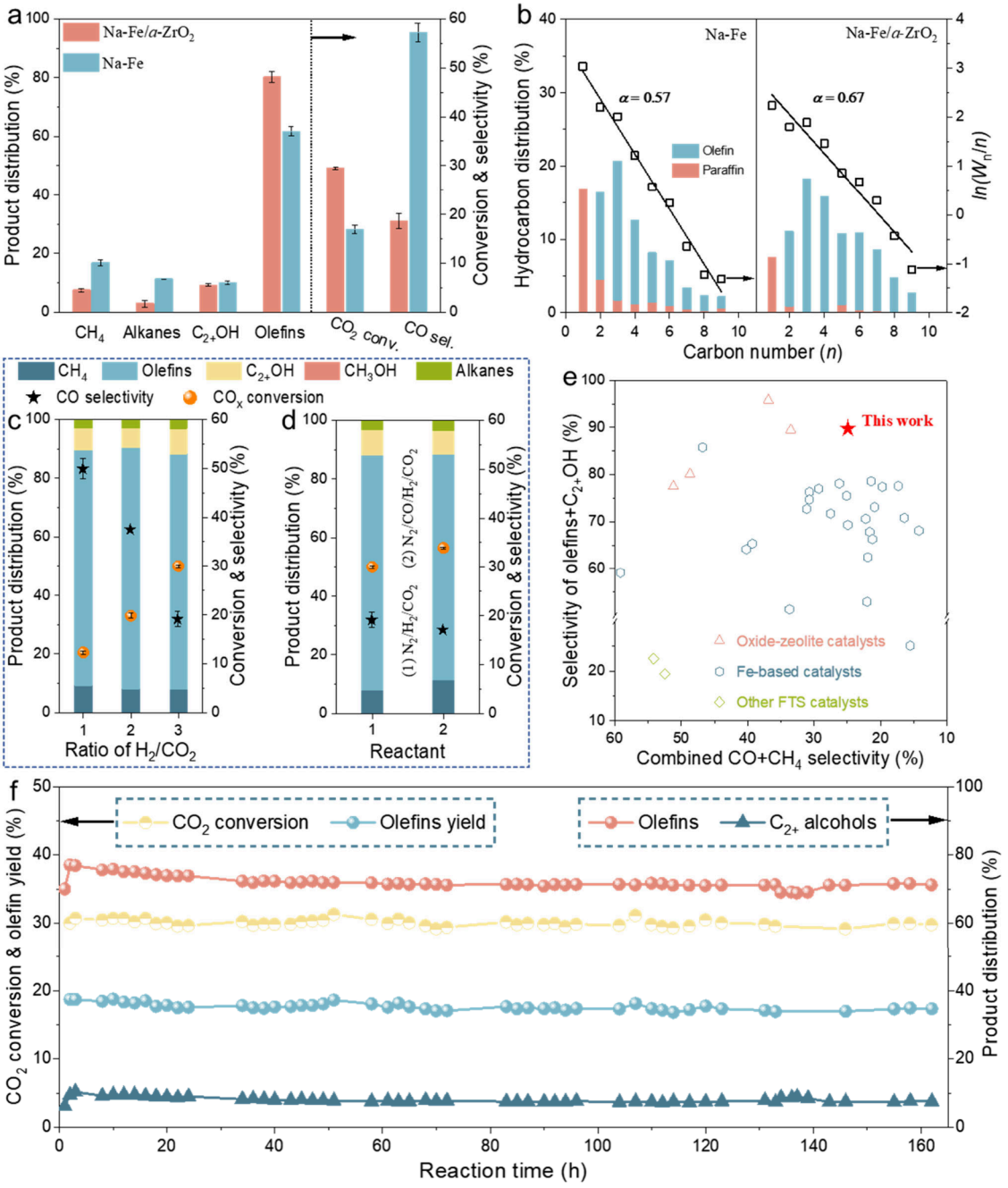


Figure 2. Catalytic performance toward CO_2 hydrogenation over Fe-based catalysts. (a) Product distribution, CO_2 conversion, and CO selectivity. (b) Detailed alkane and olefin distribution, Anderson-Schulz-Flory plot, and corresponding α value (α represents the probability of chain growth) of Na−Fe (left) and Na−Fe/*a*-ZrO_2 (right). The effect of (c) H_2/CO_2 ratio and (d) CO additive (4 vol %) in the feeding gas on the catalytic activity over Na−Fe/*a*-ZrO_2. Reaction conditions: 1 MPa, 320 °C, and 3000 mL g_{cat}^{-1} h^{-1}. (e) Comparison of the product distribution and combined CO+CH_4 selectivity of our catalyst with other state-of-the-art catalysts under comparable conditions. (f) Time-on-stream (TOS) test of the Na−Fe/*a*-ZrO_2. Operating conditions: H_2/CO_2 as 3 by volume, 1 MPa, 320 °C, and 3000 mL g_{cat}^{-1} h^{-1}.

of 9.3% at CO_2 conversion of 29.5%, while combined CH_4+CO selectivity is below 25% with ultrahigh O/P ratio of ∼28. Among the organic products, the selectivity to ethylene is 10.2%, to propylene 18.3%, and to butenes 15.8%, with the remaining 36.1% consisting of $C_{5+}^{=}$ products (see Figure 2b and Table S1). It should be noted that although alkali metals are indispensable for olefin synthesis, introducing ZrO_x species further enhances the activity toward olefins by tuning C−O bond activation and C−C coupling (Figures 1a,b and S4). At the same Fe loading and reaction conditions, we next investigated the effect of different ZrO_2 polymorphs (monoclinic (*m*-), tetragonal (*t*-), and *a*-ZrO_2) on olefin synthesis. As seen in Figures S6−S7, utilizing *m*-ZrO_2 as the support is unfavorable for CO_2/CO conversion and C−C coupling, resulting in low CO_2 conversion (12.7%), high CO selectivity (74.9%), and an α value of only 0.45. Replacing the support with *t*-ZrO_2 transforms the selectivity toward paraffins (80.9%, including 26.7% CH_4 selectivity) at a CO_2 conversion of 31.6%, suggesting that this catalyst favors alkylation reactions over olefin synthesis. These comparative studies demonstrate

https://doi.org/10.1021/jacs.6c02733
J. Am. Chem. Soc. 2026, 148, 19925−19935

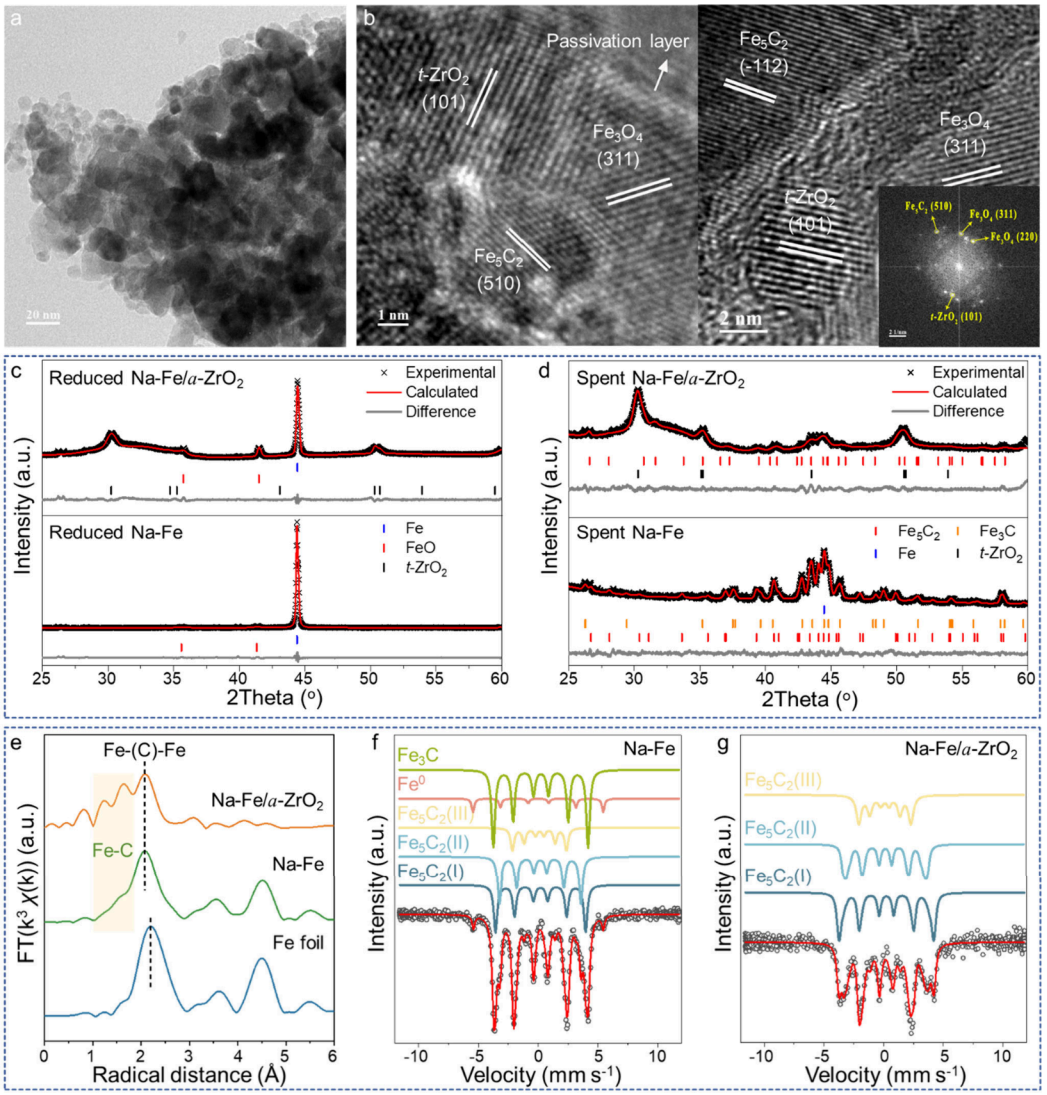


Figure 3. Structural characterizations of Fe-based catalysts. (a,b) TEM and high-resolution TEM images of the Na−Fe/*a*-ZrO_2. Rietveld refinement of *in situ* XRD patterns of (c) reduced and (d) spent catalysts. (e) The k^3-weighted Fourier-transformed EXAFS of Fe-based catalysts. *In situ* ^{57}Fe Mössbauer spectra of (f) Na−Fe and (g) Na−Fe/*a*-ZrO_2. Reaction conditions: CO_2+H_2 (H_2/CO_2 as 3 by volume), 320 °C for 5 h, and 20 bar.

the significant advantages of *a*-ZrO_2 in promoting C−C coupling to form olefins, as further corroborated by the catalytic performance of Fe-based catalysts supported on various carriers (i.e., SiO_2, ZnO, and Al_2O_3; see Figure S6).

To assess the robustness of Na−Fe/*a*-ZrO_2, we varied the H_2/CO_2 ratio, reaction pressure, and gas hourly space velocity (GHSV) in the testing. As the H_2/CO_2 ratio varies from 1 to 3, the olefin selectivity changes very slightly (82.4% to 80.3%). A higher H_2/CO_2 ratio contributes to higher CO_2 conversion (Figure 2c) and thus higher olefin STY (Figure S9). Elevating the pressure from 1 to 3 MPa (H_2/CO_2 = 3) favors CO_2 conversion to yield more olefins, leading to a gradual increase in CO_2 conversion and a decrease in CO selectivity, with only minor variations in olefin and C_{2+}OH selectivity (Figure S10). Increasing the GHSV from 3000 to 6000 mL g_{cat}^{-1} h^{-1} (H_2/CO_2 = 3, 1 MPa) maintains nearly constant olefin selectivity with O/P ratio of 25−28 (Figure S11). However, the CO_2 conversion decreases from 29.5% to 26.4%, and CO selectivity increases from 18.7% to 28.6% due to reduced contact time, indicating CO's role as an intermediate in olefin synthesis. Accordingly, cofeeding 4 vol % CO enhances olefin productivity from 19.3% to 21.6% (Figures 2d and S12), indicating that the catalyst is broadly suitable for CO_2/CO cofeeding scenarios relevant to industrial applications. Collectively, these results demonstrate that olefin selectivity is insensitive to variations in H_2/CO_2 ratio, pressure, and GHSV, highlighting the high robustness of Na−Fe/*a*-ZrO_2 across a wide range of reaction conditions.

We benchmarked our Na−Fe/*a*-ZrO_2 catalyst against state-of-the-art catalytic systems reported in the literature (Figures 2e and S13 and Table S3). The Na−Fe/*a*-ZrO_2 not only achieves extraordinary selectivity toward olefins plus valuable C_{2+}OH (~90% of total organic products) while maintaining ultrahigh O/P ratio (~28) and lowering combined CO+CH_4 selectivity to below 25%, suggesting potential cost reductions in hydrogen feedstocks and downstream processing. In contrast, previously reported Fe-based, other FTS, and oxide-zeolite catalysts generally exhibit either relatively low olefin selectivity or high selectivity toward C_1 byproducts (>35%), with typical O/P ratios below 10 under the comparable

https://doi.org/10.1021/jacs.6c02733
J. Am. Chem. Soc. 2026, 148, 19925−19935

reaction conditions. Further, we assessed the stability of the Na−Fe/*a*-ZrO_2 catalyst at 320 °C and 1 MPa. During a 162-h time-on-stream (TOS) test, the Na−Fe/*a*-ZrO_2 maintains stable CO_2 conversion with only minor fluctuations in olefin and C_{2+}OH selectivity (Figure 2f). By comparison, the unpromoted Na−Fe underwent rapid deactivation within 24 h (Figure S14), highlighting the critical role of the *a*-ZrO_2 support in enhancing stability. Thus, the Na−Fe/*a*-ZrO_2 demonstrates robust performance for CO_2 hydrogenation to olefins and C_{2+}OH, demonstrating strong potential for industrial implementation.

Structural Evolution and Characterizations

To investigate the structural evolution of Fe phases during CO_2 hydrogenation, we employed multiple structural characterizations. TEM images of spent Na−Fe/*a*-ZrO_2 reveal dense agglomerates of irregular nanoparticles forming a porous structure (Figure 3a and Table S2). High-resolution TEM images (Figures 3b and S15) further identify characteristic lattice parameters corresponding to *t*-ZrO_2 (101), Fe_3O_4 (311) and (220), and Hägg carbides (χ-Fe_5C_2) (−112) and (510) facets. ZrO_2 maintains intimate contact with Fe species, leading to the formation of abundant Fe-ZrO_2 interfaces. These interfacial interactions are further substantiated by X-ray photoelectron spectroscopy (XPS) analysis (Figures S16−S18), which demonstrates electron transfer among Na, Fe, and Zr species. Such electronic interactions are widely recognized to facilitate the formation of FeC_x-containing interfaces during catalysis.[25−28] Given the inevitable oxidation of iron-based catalysts upon exposure to air in the *ex situ* characterization process, we conducted *in situ* X-ray diffraction (XRD) and Rietveld refinement to more accurately monitor real-time structural changes. The *in situ* XRD patterns and the corresponding Rietveld refinement show that almost only metallic α-Fe is observed in the unpromoted Na−Fe after reduction in pure H_2 at 400 °C for 2 h (Figures 3c and S19). In contrast, the dynamic XRD patterns of Na−Fe/*a*-ZrO_2 under identical conditions reveal characteristic peaks corresponding to FeO, metallic α-Fe, and *t*-ZrO_2. This suggests that strong metal−support interactions inhibit the excessive reduction of FeO_x to α-Fe under a hydrogen atmosphere.[29] Upon switching to the CO_2/H_2 reactants, the α-Fe phase in the Zr-free Na−Fe is partially carburized into χ-Fe_5C_2 (Figures 3d and S19), with residual α-Fe diffraction persisting. Conversely, the *in situ* XRD and the corresponding Rietveld refinement results for Na−Fe/*a*-ZrO_2 (Figures 3d and S20) show that iron species rapidly convert to χ-Fe_5C_2, and *a*-ZrO_2 transforms to thermodynamically unstable *t*-ZrO_2. This *t*-ZrO_2 phase can be stabilized by active metals that can be trapped by the ZrO_2 lattice during the reaction, a process that simultaneously constructs defective ZrO_x with abundant oxygen vacancies.[30,31] To further validate the role of ZrO_x in regulating the carburization of iron species, we introduced a small amount of ZrO_x species into the Na−Fe system. The results indicate that atomically dispersed ZrO_x species also regulate the *in situ* evolution of Fe phases, promoting the formation of χ-Fe_5C_2 during CO_2 hydrogenation (Figure S21). These findings confirm the role of ZrO_x in tailoring the *in situ* carburization to favor χ-Fe_5C_2 generation, which would promote the conversion of CO_2 to olefins through the FTS process.

To probe amorphous or poorly crystalline α-Fe and FeC_x species, we next performed multiple spectroscopic techniques. Fe K-edge extended X-ray absorption fine structure (EXAFS) spectra (Figure S22) show predominant Fe−Fe scattering in the signals at 2.20 Å for all reduced catalysts, characteristic of metallic iron.[20,32] Fourier transform (FT)-EXAFS spectra of both spent Na−Fe and Na−Fe/*a*-ZrO_2 exhibit similar R-space structures, featuring a prominent first-shell Fe−C−Fe scattering peak at ∼2.08 Å (Figure 3e),[33] consistent with the presence of FeC_x identified by *in situ* XRD. Notably, the Na−Fe/*a*-ZrO_2 exhibits an additional distinct Fe−C scattering peak at 1.50 Å,[34,35] attributable to changes in Fe−C bonds within FeC_x species interacted with ZrO_x that also maximize the amounts of FeC_x-ZrO_x interfaces. The assignment is strongly supported by comparative EXAFS analysis of Na−Fe and ZrO_x/Na−Fe catalysts (Figures S23−S24 and Tables S4−S5). To further investigate the role of ZrO_x in modulating the structural evolution of iron phase, we employed *in situ* ^{57}Fe Mössbauer spectroscopy to identify the types of FeC_x species. Quantitative analysis (Figure 3f,g and Table S6) shows that iron species in the unpromoted Na−Fe consist of 5% α-Fe, 38% θ-Fe_3C, and 57% Hägg carbides (χ-Fe_5C_2).[5,36] In stark contrast, introducing ZrO_2 results in χ-Fe_5C_2 accounting for 100% of the iron species, with no detectable metallic Fe or other FeC_x phases remaining. The absence of θ-Fe_3C and α-Fe indicates that ZrO_2 promotes the *in situ* carburization of carbon-deficient iron species, specifically directing it toward the thermodynamically more stable χ-Fe_5C_2 phase during catalysis, in line with carbon potential theory.[37] This modulation effect contributes to the formation of abundant Fe_5C_2−ZrO_x interfaces that also enhance the catalytic performance over time, correlating well with its observed activity (Figure 2f).

To further elucidate the effect of different ZrO_2 polymorphs on the catalyst structure, we conducted a series of control experiments. EXAFS spectra of both spent Na−Fe/*m*-ZrO_2, Na−Fe/*t*-ZrO_2, and Na−Fe/*a*-ZrO_2 also exhibit similar R-space structures with a prominent first-shell Fe−C−Fe scattering peak at ∼2.08 Å,[33] consistent with the presence of FeC_x identified by *ex situ* XRD and XPS (Figure S25). For deeper insight, we also employed *in situ* ^{57}Fe Mössbauer spectroscopy to identify the types of FeC_x species. Quantitative analysis (Figures 3g and S25 and Table S6) shows that the iron species in Na−Fe/*m*-ZrO_2 consist of 12% θ-Fe_3C and 88% Hägg carbide (χ-Fe_5C_2).[5,36] In comparison, Na−Fe/*t*-ZrO_2 and Na−Fe/*a*-ZrO_2 exhibit exclusively χ-Fe_5C_2 among the iron species. The absence of other Fe species suggests that both *t*-ZrO_2 and *a*-ZrO_2 promote the *in situ* carburization of iron species. These results point to strong interactions between ZrO_2 and Fe species in the two samples, as supported by the above discussion. It is worth noting that although *t*-ZrO_2 also favors exclusive χ-Fe_5C_2 formation, the resulting Na−Fe/*t*-ZrO_2 exhibits much higher selectivity for methane and C_{2+} alkanes than Na−Fe/*a*-ZrO_2. This performance difference cannot be explained by the FeC_x phase alone, despite its critical role in dissociative CO activation. Instead, XPS and CO-probed IR spectra reveal that Na−Fe/*a*-ZrO_2 possesses a significantly higher active site density and enhanced CO adsorption capability than Na−Fe/*t*-ZrO_2 (Figure S6), likely due to the higher surface area and abundant metal nodes of amorphous ZrO_2 (Figure S1). Further, the absence of CO adsorption signals and the lowest CO_2 conversion are observed in the Na−Fe/*m*-ZrO_2 systems (Figures S6 and S25), which confirms the advantage of amorphous ZrO_2 in generating extra sites that modulate the activation models of surface-bound

https://doi.org/10.1021/jacs.6c02733
J. Am. Chem. Soc. 2026, 148, 19925−19935

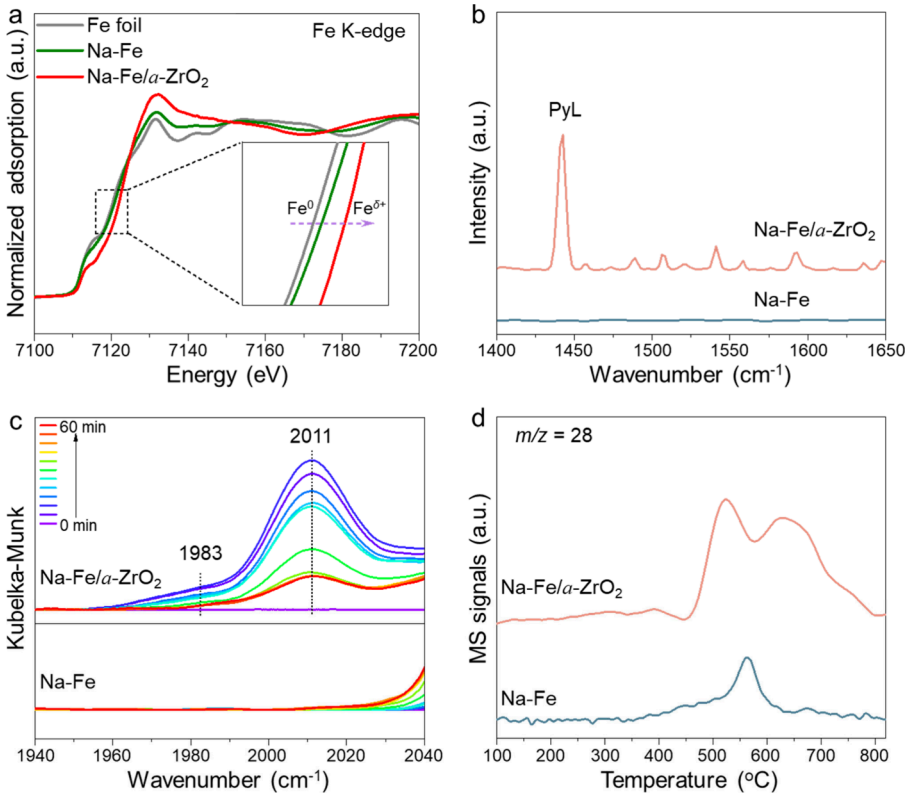


Figure 4. Identification of the active sites for CO_2 hydrogenation over Fe-based catalysts. (a) ZrO_x-induced changes of the Fe K-edge XANES spectra of Fe-based catalyst following CO_2+H_2 treatment at 1 MPa. (b) Pyridine-IR spectra, (c) CO−DRIFTS spectra of (top) Na−Fe/*a*-ZrO_2 and (bottom) Na−Fe, and (d) MS signal of m/z = 28 in CO preadsorbed TPSR-MS profiles under 5 vol % H_2/Ar flow.

*CO. Therefore, we conclude that the key role of amorphous ZrO_2 not only lies in promoting carbon-rich χ-Fe_5C_2 formation but, more importantly, in inducing abundant active sites, thus enhancing the activity for CO_2 hydrogenation to olefins.

Based on the structural characterizations, we delineate the structural evolution of Fe species on Na−Fe/*a*-ZrO_2 during reaction. Following reduction in H_2 stream, Fe_2O_3 transforms into FeO_x and metallic α-Fe. Upon switching to a CO_2/H_2 feed gas, surface Fe species undergo complete carburization into carbon-rich χ-Fe_5C_2. Furthermore, amorphous ZrO_2 modulates the reaction-induced structural evolution of the active Fe phases. This favors the formation of abundant Fe_5C_2−ZrO_x interfaces that regulate the activation behaviors of *CO intermediates, facilitating efficient C−C coupling and thereby boosting olefin synthesis.

Identifying the Active Sites

To gain deeper insight into the nature of active centers during the CO_2 hydrogenation process, we performed Fe K-edge X-ray absorption near-edge structure (XANES) measurements (Figure 4a). Compared to the Fe foil, the absorption edges for both Na−Fe and Na−Fe/*a*-ZrO_2 shift to higher energies, indicating the oxidized state of iron species. Notably, the shoulder peak at ∼7114 eV near the Fe K-edge onset, resembling that of metallic Fe foil, is more intense in Na−Fe than in Na−Fe/*a*-ZrO_2. Moreover, the absorption edge for Na−Fe/*a*-ZrO_2 occurs at a higher energy, further confirming the presence of $Fe^{\delta+}$ species. These species arise from electron transfer from iron to ZrO_x at their interfaces. The strong interfacial interactions facilitate the *in situ* carbonization of iron to form the χ-Fe_5C_2 phase during catalysis, as confirmed by *in situ* XRD and *in situ* ^{57}Fe Mössbauer spectroscopy. Zr 3d XPS spectra (Figure S26) show two peaks at 184.7 and 182.4 eV for all samples, corresponding to Zr^{4+} species.[24,38] Upon Fe and Na loading, the main Zr 3d binding energy shifts negatively, which can be attributed to the electron transfer from Fe or Na to ZrO_2. This likely modifies the coordination structure of ZrO_x and generates more defects at the metal-ZrO_x interfaces.[39] O 1s XPS spectra (Figure S27) show an increased fraction of oxygen vacancies after alkali metal doping, implying the formation of undercoordinated $Zr^{\delta+}$ sites following O atom removal from ZrO_2 under a reduction atmosphere. Furthermore, pyridine-IR spectra (Figure 4b) show a strong IR band for Lewis acidic sites (LAS) in Na−Fe/*a*-ZrO_2, while the unpromoted Na−Fe exhibits no significant LAS signal.[24] This further confirms that strong interfacial interactions enhance the exposure of coordinatively unsaturated ZrO_x sites. Such sites are likely to modulate the adsorption/activation of weakly basic CO molecules, promoting their conversion into olefins and higher alcohols via the CO insertion route.

We next performed CO_2 and CO pulse transient hydrogenation (PTH) experiments to elucidate the role of unsaturated ZrO_x species in modulating C−O bond activation behaviors. Compared to Na−Fe, distinct peaks for both ethylene (C_2H_4) and propylene (C_3H_6) are also observed on Na−Fe/*a*-ZrO_2, while the intensity of CH_4 sharply decreases (Figures S28−S29). This shift indicates preferential conversion of CO_2 and CO to olefins via C−C coupling rather than to CH_4 on Zr-modulated iron-based catalysts, supporting the strong modulation effect of unsaturated ZrO_x sites on CO activation modes and subsequent C−C coupling reactions.

To further elucidate the role of undercoordinated $Zr^{\delta+}$ sites in CO_2 hydrogenation to olefins, we next performed *in situ*

https://doi.org/10.1021/jacs.6c02733
J. Am. Chem. Soc. 2026, 148, 19925−19935

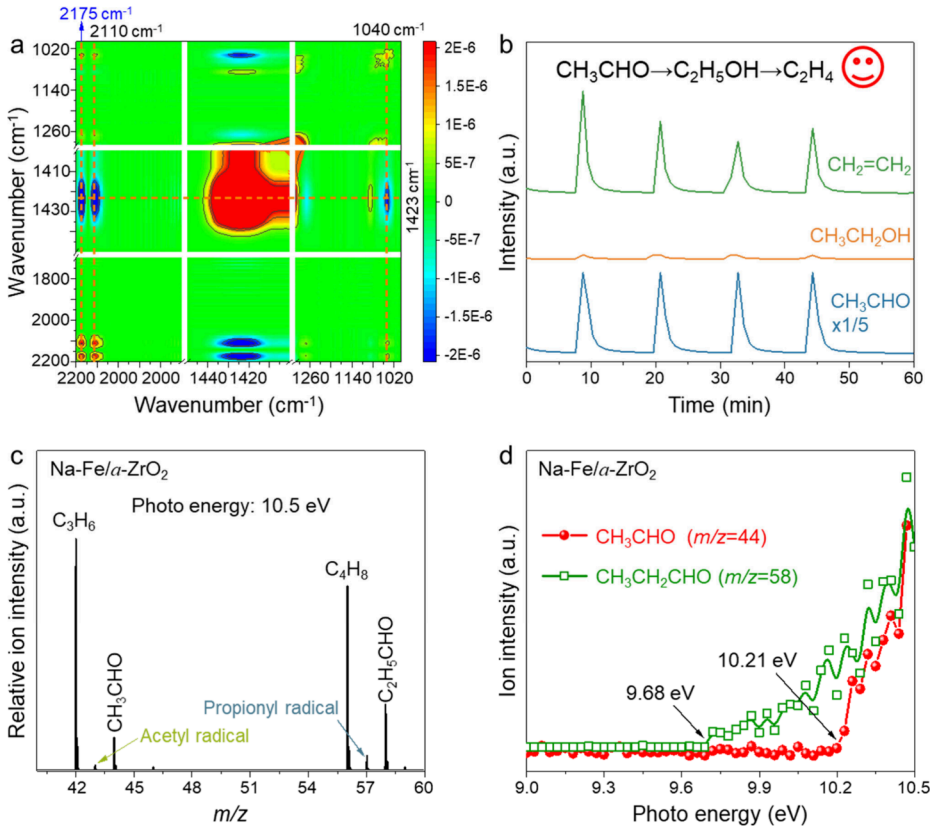


Figure 5. Characterization and evolution of active intermediates. (a) Two-dimensional correlation IR synchronous maps in the region of 1000−2200 cm^{-1}. Color coding indicates the correlation between the respective intermediates. Conditions: Na−Fe/*a*-ZrO_2, 250 °C, 4 bar, H_2/CO_2 = 3, ca. 10 mL min^{-1}. (b) Mass signals of CH_3CH_2OH and C_2H_4 after pulsing CH_3CH_2OH over spent Na−Fe/*a*-ZrO_2 in a 5 vol % H_2/Ar stream at 320 °C. (c) *In situ* SVUV-PIMS signals of desorbed species during the CO_2 hydrogenation and (d) photoionization efficiency spectra for the signals of desorbed CH_3CHO (m/z = 44) and CH_3CH_2CHO (m/z = 58) over the Na−Fe/*a*-ZrO_2. Operation conditions: 320 °C and 5.8 bar.

diffuse reflectance infrared Fourier transform spectroscopy (DRIFTS) using CO as a probe molecule. Observed bands at 1983 and 2011 (2005) cm^{-1} are assigned to bridge-bonded and linearly adsorbed *CO, respectively.[40,41] Notably, Na-ZrO_2 exhibits stronger *CO signals compared to sole ZrO_2, suggesting that interfacial unsaturated ZrO_x sites provide abundant adsorption sites for CO molecules (Figure S30). Significantly, exposing the Na−Fe/*a*-ZrO_2 to CO under identical conditions shows intensified CO adsorption bands accompanied by a blue shift in the peak positions (Figures 4c and S30). This observation indicates the existence of more unsaturated ZrO_x sites due to the strong electronic interactions, as corroborated by XPS, XANES, and *in situ* XRD analyses, further enhancing nondissociative CO activation to induce higher surface coverage of this intermediate. In stark contrast, the unpromoted Na−Fe exhibits no significant CO adsorption bands and high CO selectivity, suggesting that the absence of unsaturated ZrO_x sites may impede CO conversion due to weakened CO adsorption, consistent with the catalytic performance and active site analysis of Na−Fe/*m*-ZrO_2 (Figures S6 and S25). As per our previous work,[24] the strong synergy between metals and ZrO_2 promotes the formation of coordinatively unsaturated $Zr^{\delta+}$ cations adjacent to oxygen defects, significantly improving CO adsorption, particularly of nondissociative CO species, and thereby facilitating subsequent CO insertion reactions. Notably, introducing a small amount of unsaturated ZrO_x species onto the Na−Fe also enhances both the nondissociative activation ability of *CO and the activity in olefin synthesis (see Figures S3 and S31−S37 and Table S7 for details). We then performed CO-preadsorbed TPSR-MS experiments to further investigate the critical role of coordinatively unsaturated Zr species in governing CO activation modes. As shown in Figure 4d, Na−Fe/*a*-ZrO_2 displays markedly higher molecular *CO desorption compared to Na−Fe, indicating a significant enhancement in nondissociative *CO activation attributed to the formation of abundant unsaturated Zr species. The enhanced nondissociative *CO adsorption capacity, also supported by the CO−DRIFTS spectra (Figure 4c), is a crucial prerequisite for CO insertion. The enhanced ability for nondissociative CO activation raises the coverage of surface-bound *CO, increasing the probability of its coupling with alkyl species and ultimately facilitating efficient C−C coupling reactions.[27,42]

Chain propagation in Fischer−Tropsch synthesis (FTS) typically involves CO insertion and carbide mechanisms.[5,43] Iron carbides (e.g., χ-Fe_5C_2) are generally regarded as active sites for *CO dissociative adsorption and carbon chain growth via the carbide mechanism.[6,12,19,44] Conversely, nondissociative *CO adsorption promotes CO insertion reactions, recognized as a promising route for higher alcohol (HA) synthesis over Fe-based catalysts.[5,24,27,33] Based on complementary characterization techniques for identifying active sites, we propose that unsaturated ZrO_x sites facilitate nondissociative CO activation, thereby boosting C−C coupling reactions. Specifically, CO insertion into alkyl species appears at the interfaces between

https://doi.org/10.1021/jacs.6c02733
J. Am. Chem. Soc. 2026, 148, 19925−19935

Fe_5C_2 and unsaturated ZrO_x sites, which promotes the synthesis of HA intermediates, as evidenced by detectable C_{2+} oxygenates under reaction conditions (Figure 2). The resulting HA can then undergo dehydration over the LAS sites to form olefins, thereby boosting olefin production.[6,45,46] Thus, the CO insertion mechanism driven by unsaturated ZrO_x sites adjacent to Fe_5C_2 phases enables efficient C−C coupling reactions, ultimately leading to the selective olefin synthesis from CO_2 hydrogenation.

Mechanistic Studies

To elucidate the origin of the high selectivity for both olefins and C_{2+} oxygenates, we next performed *in situ* DRIFTS analysis during catalysis. As shown in Figure S38, the bands of olefins (3050−3150 cm^{-1}) and alkanes (2900−3000 cm^{-1}) are observed immediately upon introducing the reactants (CO_2/H_2) into the *in situ* DRIFTS cell.[21,47] Concurrently, bands assigned to gaseous CO, HCOO*, and $*CO_3$ species are detected (Figure S39), indicating the transformation of adsorbed CO_2 to CO via the RWGS process. The formed *CO can then be rapidly converted into adsorbed CH_x species, which subsequently produce paraffins and olefins via the carbide mechanism over FeC_x sites.[19,20,44,47] Notably, the carbide mechanism does not generate C_{2+} oxygenates through the polymerization of CH_x species.[48] Interestingly, bands corresponding to $*CH_3CHO$ occur and intensify over time, coinciding with a decline in gaseous CO and CH_4 signals after 60 min of reactant exposure (Figures S38−S39). This intermediate is typically associated with C−C coupling between CH_x and *CO species through the CO insertion route.[49,50] To further probe this route, we employed two-dimensional correlation IR spectroscopy to monitor the relationships between intermediates. The color-coded results provide a visual representation of their interactions and reaction pathways. Figure 5a shows a negative correlation between CO and $*CH_3CHO$ signals (around 2100−2200 cm^{-1} and 1423 cm^{-1}, respectively), indicating the conversion of *CO into $*CH_3CHO$. Furthermore, similar negative correlations are observed between $*CH_3CHO$ and $*CH_3CH_2O$ species, supporting the proposed formation of these intermediates through CO insertion into alkyl species. These findings collectively confirm the presence of a CO insertion mechanism over Na−Fe/*a*-ZrO_2.

To verify olefin formation via C_{2+} oxygenated intermediates, we conducted pulse transient hydrogenation experiments using CH_3CHO and CH_3CH_2OH over the Na−Fe/*a*-ZrO_2 catalyst. As shown in Figure S40, MS signals corresponding to CH_3CH_2OH and C_2H_4 are clearly observed upon exposing the catalyst to CH_3CHO vapor. This indicates CH_3CHO conversion to C_2H_4 via hydrogenation to CH_3CH_2OH followed by dehydration. Moreover, the rapid conversion of CH_3CH_2OH to C_2H_4 confirms that the C_{2+} oxygenates serve as key intermediates for olefin synthesis (Figures 5b and S41). To investigate this unique C−C coupling process, we introduce a CO pulse into the CO_2/H_2 atmosphere over the Na−Fe/*a*-ZrO_2 (Figure S42). The emergence of MS signals related to various C_{2+} oxygenates and olefins suggests that CO insertion into alkyl species leads to the formation of C_{2+} oxygenated intermediates, which are then converted into olefins. Given that the unsaturated ZrO_x species are responsible for the nondissociative activation of CO species that are the prerequisite for CO insertion, we conclude that CO insertion-mediated olefin synthesis is highly associated with these defective species.

To further confirm the CO insertion path during CO_2 hydrogenation to olefins, we next conducted *in situ* synchrotron-based vacuum ultraviolet photoionization mass spectrometry (SVUV-PIMS) experiments. This technique is highly effective for identifying true reaction intermediates due to its soft ionization capability with tunable photon energy and high sensitivity to trace, short-lived desorbed species. Using a photon energy of 10.5 eV to selectively ionize oxygenated intermediates like $*CH_2CHO$ (m/z = 44) while avoiding ionization of CO_2 or C_3H_8 (also m/z = 44),[51−53] strong signals corresponding to $*CH_3CHO$ (m/z = 44) and $*CH_3CH_2CHO$ (m/z = 58) are observed. Interestingly, the signals for $*CH_3CO$ (m/z = 43) and $*CH_3CH_2CO$ (m/z = 57) radicals are also clearly detected (Figure 5c), providing direct evidence for olefin synthesis via C_{2+} oxygenated intermediates. Furthermore, when the photon energy is scanned from 9.0 to 10.6 eV, distinct ionization thresholds appear at 10.21 and 9.68 eV (Figure 5d), assignable to desorbed $*CH_3CH_2CHO$ and $*CH_3CHO$, respectively. The observations support the CO insertion route as a key mechanism for chain growth over the Na−Fe/*a*-ZrO_2.

To investigate the mechanism underlying the high olefin selectivity of Na−Fe/*a*-ZrO_2, we selected C_2H_4 as a representative olefin and conducted temperature-programmed desorption (TPD) and pulse transient hydrogenation (PTH) experiments to determine whether olefins preferentially desorb or undergo secondary hydrogenation. The C_2H_4-TPD profiles (Figure S43) reveal that the main desorption peak for Na−Fe/*a*-ZrO_2 occurs at approximately 420 °C, significantly lower than the peak at ∼530 °C observed for the unpromoted Na−Fe. This decrease in desorption temperature is attributed to the absence of Fe^0 sites in Na−Fe/*a*-ZrO_2, as evidenced by *in situ* ^{57}Fe Mössbauer spectroscopy (Figure 3f,g). Since Fe^0 sites typically serve as active centers for secondary hydrogenation of olefins,[54] their absence reduces the likelihood of this reaction and promotes olefins desorption as final products. In the PTH experiments, we introduced C_2H_4 gas into the reactor along with 5 vol % H_2/Ar stream at 320 °C. The conversion of C_2H_4 to ethane (C_2H_6) was monitored by mass spectrometry. As shown in Figure S44, the ratio of C_2H_4 to C_2H_6 integral peak areas increases from 22.4 for Na−Fe to 71.2 for Na−Fe/*a*-ZrO_2. Importantly, the C_2H_4 to C_2H_6 peak area ratio exhibits a positive correlation with the olefin/alkane ratio in the products (Figure S45). This correlation further underscores the effective suppression of secondary hydrogenation of olefins to alkanes, facilitated by the modulation effects of ZrO_x species on the *in situ* carbonization of iron species, which is essential for achieving high olefin selectivity.

CONCLUSIONS

In summary, we have developed a simple yet effective strategy to enhance the performance of CO_2-modified Fischer−Tropsch synthesis toward olefins by incorporating unsaturated ZrO_x sites into iron catalysts. These unsaturated ZrO_x sites engage in electronic interactions with Fe centers and effectively modulate C−O bond activation, selectively promoting C−C coupling between *CO and alkyl intermediates while significantly suppressing olefin rehydrogenation. Operating at 1 MPa and 320 °C, the optimized catalyst achieves high selectivity toward olefins and higher alcohols (up to 89.6%), along with an ultrahigh olefin-to-paraffin (O/P) ratio (∼28)

https://doi.org/10.1021/jacs.6c02733
J. Am. Chem. Soc. 2026, 148, 19925−19935

and a low combined CO+CH_4 selectivity (~25%), surpassing most reported catalytic systems to date. Multimodal *in situ/operando* spectroscopic and chemisorption-pulse experiments further reveal that unsaturated ZrO_x sites promote the preferential nondissociative activation of surface-bound *CO and drive *CO insertion into alky species, thereby facilitating olefin production through C_{2+} oxygenated intermediates. Furthermore, the catalyst exhibits high stability for over 160 h, highlighting its potential for industrial applications. This work provides a promising strategy for hydrogen-efficient CO_2 conversion into synthetic chemicals and fuels, contributing to the development of a sustainable circular economy.

■ ASSOCIATED CONTENT

Supporting Information

The Supporting Information is available free of charge at https://pubs.acs.org/doi/10.1021/jacs.6c02733.

Additional catalytic activity and XRD patterns, N_2 sorption isotherms, XPS spectra, XAS spectra, TEM images, TPR/TPD profiles, TPSR-MS profiles, chemsorption-pulse experiments, and *in situ* DRIFTS spectra (PDF)

■ AUTHOR INFORMATION

Corresponding Authors

Guangchao Li − *Department of Applied Biology and Chemical Technology, The Hong Kong Polytechnic University, Hong Kong 999077, P. R. China;* orcid.org/0000-0001-7521-8336; Email: guangchao.li@polyu.edu.hk

Xinlin Hong − *College of Chemistry and Molecular Sciences, Wuhan University, Wuhan 430072, P. R. China;* Email: hongxl@whu.edu.cn

Guoliang Liu − *College of Chemistry and Molecular Sciences, Wuhan University, Wuhan 430072, P. R. China; Interdisciplinary Institute of NMR and Molecular Sciences, Key Laboratory of Hubei Province for Coal Conversion and New Carbon Materials, School of Chemistry and Chemical Engineering, Wuhan University of Science and Technology, Wuhan 430081, P. R. China;* orcid.org/0000-0003-1575-254X; Email: liugl@whu.edu.cn

Anmin Zheng − *Interdisciplinary Institute of NMR and Molecular Sciences, Key Laboratory of Hubei Province for Coal Conversion and New Carbon Materials, School of Chemistry and Chemical Engineering, Wuhan University of Science and Technology, Wuhan 430081, P. R. China;* orcid.org/0000-0001-7115-6510; Email: zam@wust.edu.cn

Authors

Tangkang Liu − *College of Chemistry and Molecular Sciences, Wuhan University, Wuhan 430072, P. R. China; Interdisciplinary Institute of NMR and Molecular Sciences, Key Laboratory of Hubei Province for Coal Conversion and New Carbon Materials, School of Chemistry and Chemical Engineering, Wuhan University of Science and Technology, Wuhan 430081, P. R. China;* orcid.org/0009-0005-0714-5573

Hanjun Lu − *College of Chemistry and Molecular Sciences, Wuhan University, Wuhan 430072, P. R. China*

Wentian Niu − *Wolfson Catalysis Centre, Department of Chemistry, University of Oxford, Oxford OX1 3QR, United Kingdom*

Renzo A. Leeflang − *Wolfson Catalysis Centre, Department of Chemistry, University of Oxford, Oxford OX1 3QR, United Kingdom*

Tai-Sing Wu − *National Synchrotron Radiation Research Centre, Hsinchu 30076, Taiwan;* orcid.org/0000-0002-3285-7258

A. Iulian Dugulan − *Fundamental Aspects of Materials and Energy, Delft University of Technology, Delft JB 2629, The Netherlands*

Xianfeng Yi − *State Key Laboratory of Magnetic Resonance and Atomic and Molecular Physics, Innovation Academy for Precision Measurement Science and Technology, Chinese Academy of Sciences, Wuhan 430071, P. R. China;* orcid.org/0000-0001-9224-3111

Chengyuan Liu − *National Synchrotron Radiation Laboratory, University of Science and Technology of China, Hefei 230029, P. R. China*

Long Zhao − *National Synchrotron Radiation Laboratory, University of Science and Technology of China, Hefei 230029, P. R. China;* orcid.org/0000-0002-6585-0028

Shik Chi Edman Tsang − *Department of Applied Biology and Chemical Technology, The Hong Kong Polytechnic University, Hong Kong 999077, P. R. China; Wolfson Catalysis Centre, Department of Chemistry, University of Oxford, Oxford OX1 3QR, United Kingdom;* orcid.org/0000-0002-8796-3146

Complete contact information is available at: https://pubs.acs.org/10.1021/jacs.6c02733

Author Contributions

The manuscript was written through the contributions of all authors. All authors have approved the final version of the manuscript.

Notes

The authors declare no competing financial interest.
S.C.E.T. is deceased (May 20, 2025).

■ ACKNOWLEDGMENTS

This work is financially supported by the National Key Research and Development Program of China (2021YFA1502600), the National Science Foundation of China (22125304, 22472126, 22172113, 22502151), Hubei Provincial Natural Science Foundation of China (2025AFA065, 2025AFA008), the Postdoctoral Fellowship Program of CPSF (GZC20232002), the Natural Science Foundation of Wuhan (2024040701010058), the Department of Science and Technology of Guangdong Province (GDSTC 2025A1515011688), and the Hong Kong Polytechnic University (P0055259, P0049034).

■ REFERENCES

(1) Ye, R.-P.; Ding, J.; Gong, W.; Argyle, M. D.; Zhong, Q.; Wang, Y.; Russell, C. K.; Xu, Z.; Russell, A. G.; Li, Q.; Fan, M.; Yao, Y.-G. CO_2 hydrogenation to high-value products *via* heterogeneous catalysis. *Nat. Commun.* **2019**, *10*, 5698.

(2) Zhou, Q.; Guo, Y.; Zhu, Y. Reticular copper dual sites embedded with semiconductor particles for selective CO_2-to-C_2H_4 photoreduction. *Nat. Catal.* **2025**, *8*, 728−739.

(3) Gao, P.; Zhang, L.; Li, S.; Zhou, Z.; Sun, Y. Novel heterogeneous catalysts for CO_2 hydrogenation to liquid fuels. *ACS Cent. Sci.* **2020**, *6*, 1657−1670.

(4) Wei, J.; Yao, R.; Han, Y.; Ge, Q.; Sun, J. Towards the development of the emerging process of CO_2 heterogeneous

hydrogenation into high-value unsaturated heavy hydrocarbons. *Chem. Soc. Rev.* **2021**, *50*, 10764−10805.
(5) Li, Z.; Wu, W.; Wang, M.; Wang, Y.; Ma, X.; Luo, L.; Chen, Y.; Fan, K.; Pan, Y.; Li, H.; Zeng, J. Ambient-pressure hydrogenation of CO_2 into long-chain olefins. *Nat. Commun.* **2022**, *13*, 2396.
(6) Ye, J.; Dimitratos, N.; Rossi, L. M.; Thonemann, N.; Beale, A. M.; Wojcieszak, R. Hydrogenation of CO_2 for sustainable fuel and chemical production. *Science* **2025**, *387*, 6737.
(7) Li, Z.; Wang, J.; Qu, Y.; Liu, H.; Tang, C.; Miao, S.; Feng, Z.; An, H.; Li, C. Highly selective conversion of carbon dioxide to lower olefins. *ACS Catal.* **2017**, *7*, 8544−8548.
(8) Wang, S.; Wu, T.; Lin, J.; Ji, Y.; Yan, S.; Pei, Y.; Xie, S.; Zong, B.; Qiao, M. Iron-potassium on single-walled carbon nanotubes as efficient catalyst for CO_2 hydrogenation to heavy olefins. *ACS Catal.* **2020**, *10*, 6389−6401.
(9) Wang, S.; Zhang, L.; Zhang, W.; Wang, P.; Qin, Z.; Yan, W.; Dong, M.; Li, J.; Wang, J.; He, L.; Olsbye, U.; Fan, W. Selective conversion of CO_2 into propene and butene. *Chem.* **2020**, *6*, 3344−3363.
(10) Guo, L.; Gao, X.; Gao, W.; Wu, H.; Wang, X.; Sun, S.; Wei, Y.; Kugue, Y.; Guo, X.; Sun, J.; Tsubaki, N. High-yield production of liquid fuels in CO_2 hydrogenation on a zeolite-free Fe-based catalyst. *Chem. Sci.* **2023**, *14*, 171−178.
(11) Xu, Y.; Zhai, P.; Deng, Y.; Xie, J.; Liu, X.; Wang, S.; Ma, D. Highly selective olefin production from CO_2 hydrogenation on iron catalysts: A subtle synergy between manganese and sodium additives. *Angew. Chem., Int. Ed.* **2020**, *59*, 21736−21744.
(12) Liang, J.; Liu, J.; Guo, L.; Wang, W.; Wang, C.; Gao, W.; Guo, X.; He, Y.; Yang, G.; Yasuda, S.; Liang, B.; Tsubaki, N. CO_2 hydrogenation over Fe-Co bimetallic catalysts with tunable selectivity through a graphene fencing approach. *Nat. Commun.* **2024**, *15*, 512.
(13) Zhang, Q.; Li, X.; Wang, S.; Wang, S.; Geng, R.; Wang, P.; Dong, M.; Chen, J.; Wang, J.; Li, X.; Olsbye, U.; Fan, W. Enhancement of CO_2 hydrogenation to light olefins by developing a higher alcohols-intermediate route. *J. Am. Chem. Soc.* **2025**, *147*, 45070−45083.
(14) Wang, X.; Zeng, T.; Guo, X.; Yan, Z.; Ban, H.; Yao, R.; Li, C.; Gu, X.; Ding, M. Breaking the activity-selectivity trade-off of CO_2 hydrogenation to light olefins. *Proc. Natl. Acad. Sci. U.S.A.* **2024**, *121*, No. e2408297121.
(15) Chen, S.; Wang, J.; Feng, Z.; Jiang, Y.; Hu, H.; Qu, Y.; Tang, S.; Li, Z.; Liu, J.; Wang, J.; Li, C. Hydrogenation of CO_2 to light olefins over $ZnZrO_x$/SSZ-13. *Angew. Chem., Int. Ed.* **2024**, *63*, No. e202316874.
(16) Wang, S.; Zhang, L.; Wang, P.; Liu, X.; Chen, Y.; Qin, Z.; Dong, M.; Wang, J.; He, L.; Olsbye, U.; Fan, W. Highly effective conversion of CO_2 into light olefins abundant in ethene. *Chem.* **2022**, *8*, 1376−1394.
(17) Yang, Q.; Fedorova, E. A.; Cao, D.; Saraçi, E.; Kondratenko, V. A.; Kreyenschulte, C. R.; Lund, H.; Bartling, S.; Weiß, J.; Doronkin, D. E.; Grunwaldt, J. D.; Brückner, A.; Jiao, H.; Kondratenko, E. V. Understanding Mn-modulated restructuring of Fe-based catalysts for controlling selectivity in CO_2 hydrogenation to olefins. *Nat. Catal.* **2025**, *8*, 595−606.
(18) Ning, S.; Wang, J.; Wu, X.; Li, L.; Zhang, S.; Chen, S.; Ren, X.; Gao, L.; Hao, Y.; Lv, C.; Li, Y.; Ye, J. Natural sunlight-driven CO_2 hydrogenation into light olefins at ambient pressure over bifunctional Cu-promoted CoFe alloy catalyst. *Adv. Funct. Mater.* **2024**, *34*, 2400798.
(19) Zhang, C.; Xu, M.; Yang, Z.; Zhu, M.; Gao, J.; Han, Y. Uncovering the electronic effects of zinc on the structure of Fe_5C_2-ZnO catalysts for CO_2 hydrogenation to linear α-olefins. *Appl. Catal., B* **2021**, *295*, 120287.
(20) Lopez Luna, M.; Timoshenko, J.; Kordus, D.; Rettenmaier, C.; Chee, S. W.; Hoffman, A. S.; Bare, S. R.; Shaikhutdinov, S.; Roldan Cuenya, B. Role of the oxide support on the structural and chemical evolution of Fe catalysts during the hydrogenation of CO_2. *ACS Catal.* **2021**, *11*, 6175−85.
(21) Khan, M. K.; Butolia, P.; Jo, H.; Irshad, M.; Han, D.; Nam, K.-W.; Kim, J. Selective conversion of carbon dioxide into liquid hydrocarbons and long-chain α-olefins over Fe-amorphous AlO_x bifunctional catalysts. *ACS Catal.* **2020**, *10*, 10325−10338.
(22) Han, Y.; Fang, C.; Ji, X.; Wei, J.; Ge, Q.; Sun, J. Interfacing with carbonaceous potassium promoters boosts catalytic CO_2 hydrogenation of iron. *ACS Catal.* **2020**, *10*, 12098−12108.
(23) Orege, J. I.; Wei, J.; Han, Y.; Yang, M.; Sun, X.; Zhang, J.; Amoo, C. C.; Ge, Q.; Sun, J. Highly stable Sr and Na co-decorated Fe catalyst for high-valued olefin synthesis from CO_2 hydrogenation. *Appl. Catal., B* **2022**, *316*, 121640.
(24) Liu, T.; Xu, D.; Song, M.; Hong, X.; Liu, G. K-ZrO_2 interfaces boost CO_2 hydrogenation to higher alcohols. *ACS Catal.* **2023**, *13*, 4667−4674.
(25) Liu, Y.; Chen, B.; Liu, R.; Liu, W.; Gao, X.; Tan, Y.; Zhang, Z.; Tu, W. CO_2 hydrogenation to olefins on supported iron catalysts: Effects of support properties on carbon-containing species and product distribution. *Fuel* **2022**, *324*, 124649.
(26) Barrios, A. J.; Peron, D. V.; Chakkingal, A.; Dugulan, A. I.; Moldovan, S.; Nakouri, K.; Thuriot-Roukos, J.; Wojcieszak, R.; Thybaut, J. W.; Virginie, M.; Khodakov, A. Y. Efficient promoters and reaction paths in the CO_2 hydrogenation to light olefins over zirconia-supported iron catalysts. *ACS Catal.* **2022**, *12*, 3211−3225.
(27) Yao, R.; Wei, J.; Ge, Q.; Xu, J.; Han, Y.; Ma, Q.; Xu, H.; Sun, J. Monometallic iron catalysts with synergistic Na and S for higher alcohols synthesis *via* CO_2 hydrogenation. *Appl. Catal., B* **2021**, *298*, 120556.
(28) Zhai, P.; Xu, C.; Gao, R.; Liu, X.; Li, M.; Li, W.; Fu, X.; Jia, C.; Xie, J.; Zhao, M.; Wang, X.; Li, Y.-W.; Zhang, Q.; Wen, X.-D.; Ma, D. Highly tunable selectivity for syngas-derived alkenes over zinc and sodium-modulated Fe_5C_2 catalyst. *Angew. Chem., Int. Ed.* **2016**, *55*, 9902−9907.
(29) Wan, H.; Wu, B.; Xiang, H.; Li, Y. Fischer−Tropsch synthesis: Influence of support incorporation manner on metal dispersion, metal-support interaction, and activities of iron catalysts. *ACS Catal.* **2012**, *2*, 1877−1883.
(30) Samson, K.; Śliwa, M.; Socha, R. P.; Góra-Marek, K.; Mucha, D.; Rutkowska-Zbik, D.; Paul, J.-F.; Ruggiero-Mikołajczyk, M.; Grabowski, R.; Słoczyński, J. Influence of ZrO_2 structure and copper electronic state on activity of Cu/ZrO_2 catalysts in methanol synthesis from CO_2. *ACS Catal.* **2014**, *4*, 3730−3741.
(31) Wang, W.; Qu, Z.; Song, L.; Fu, Q. CO_2 hydrogenation to methanol over Cu/CeO_2 and Cu/ZrO_2 catalysts: Tuning methanol selectivity *via* metal-support interaction, J. *Energy Chem.* **2020**, *40*, 22−30.
(32) Chang, Q.; Zhang, C.; Liu, C.; Wei, Y.; Cheruvathur, A. V.; Dugulan, A. I.; Niemantsverdriet, J. W.; Liu, X.; He, Y.; Qing, M.; Zheng, L.; Yun, Y.; Yang, Y.; Li, Y. Relationship between iron carbide phases (ε-Fe_2C, Fe_7C_3, and χ-Fe_5C_2) and catalytic performances of Fe/SiO_2 Fischer−Tropsch catalysts. *ACS Catal.* **2018**, *8*, 3304−3316.
(33) Zhang, Q.; Wang, S.; Geng, R.; Wang, P.; Dong, M.; Wang, J.; Fan, W. Hydrogenation of CO_2 to higher alcohols on an efficient Cr-modified CuFe catalyst. *Appl. Catal., B* **2023**, *337*, 123013.
(34) Yang, Q.; Kondratenko, V. A.; Petrov, S. A.; Doronkin, D. E.; Saraci, E.; Lund, H.; Arinchtein, A.; Kraehnert, R.; Skrypnik, A. S.; Matvienko, A. A.; Kondratenko, E. V. Identifying performance descriptors in CO_2 hydrogenation over iron-based catalysts promoted with alkali metals. *Angew. Chem., Int. Ed.* **2022**, *61*, No. e202116517.
(35) Wang, Y.; Wang, K.; Zhang, B.; Peng, X.; Gao, X.; Yang, G.; Hu, H.; Wu, M.; Tsubaki, N. Direct conversion of CO_2 to ethanol boosted by intimacy-sensitive multifunctional catalysts. *ACS Catal.* **2021**, *11*, 11742−11753.
(36) Lu, F.; Chen, X.; Lei, Z.; Wen, L.; Zhang, Y. Revealing the activity of different iron carbides for Fischer−Tropsch synthesis. *Appl. Catal., B* **2021**, *281*, 119521.
(37) de Smit, E.; Cinquini, F.; Beale, A. M.; Safonova, O. V.; van Beek, W.; Sautet, P.; Weckhuysen, B. M. Stability and reactivity of ϵ-χ-θ iron carbide catalyst phases in Fischer−Tropsch synthesis: Controlling μ_c. *J. Am. Chem. Soc.* **2010**, *132*, 14928−14941.

https://doi.org/10.1021/jacs.6c02733
J. Am. Chem. Soc. 2026, 148, 19925−19935

(38) Vergara, T.; Gómez, D.; Warmuth, L.; Enss, A. E.; Peterlechner, M.; Pallacán, R.; Diaconescu, V. M.; Simonelli, L.; Studt, F.; Concepción, P.; Jiménez, R.; Karelovic, A. On the structure sensitivity of CO_2 hydrogenation over Cu/ZrO_2: Insights into the role of the support and the active sites. *ACS Catal.* **2024**, *14*, 14127−14138.
(39) Yang, C.; Pei, C.; Luo, R.; Liu, S.; Wang, Y.; Wang, Z.; Zhao, Z.-J.; Gong, J. Strong electronic oxide-support interaction over In_2O_3/ZrO_2 for highly selective CO_2 hydrogenation to methanol. *J. Am. Chem. Soc.* **2020**, *142*, 19523−19531.
(40) Xu, M.; Yao, S.; Rao, D.; Niu, Y.; Liu, N.; Peng, M.; Zhai, P.; Man, Y.; Zheng, L.; Wang, B.; Zhang, B.; Ma, D.; Wei, M. Insights into interfacial synergistic catalysis over $Ni@TiO_{2-x}$ catalyst toward water-gas shift reaction. *J. Am. Chem. Soc.* **2018**, *140*, 11241−11251.
(41) Schroter, M. K.; Khodeir, L.; Hambrock, J.; Loffler, E.; Muhler, M.; Fischer, R. A. Redox chemistry of Cu colloids probed by adsorbed CO: An *in situ* attenuated total reflection fourier transform infrared study. *Langmuir* **2004**, *20*, 9453−9455.
(42) Liu, S.; Yang, C.; Zha, S.; Sharapa, D.; Studt, F.; Zhao, Z.; Gong, J. Moderate surface segregation promotes selective ethanol production in CO_2 hydrogenation reaction over CoCu catalysts. *Angew. Chem., Int. Ed.* **2022**, *61*, No. e202109027.
(43) Davis, B. H. Fischer−Tropsch synthesis: Reaction mechanisms for iron catalysts. *Catal. Today* **2009**, *141*, 25−33.
(44) Zhu, J.; Zhang, G.; Li, W.; Zhang, X.; Ding, F.; Song, C.; Guo, X. Deconvolution of the particle size effect on CO_2 hydrogenation over iron-based catalysts. *ACS Catal.* **2020**, *10*, 7424−7433.
(45) Yarulina, I.; Chowdhury, A. D.; Meirer, F.; Weckhuysen, B. M.; Gascon, J. Recent trends and fundamental insights in the methanol-to-hydrocarbons process. *Nat. Catal.* **2018**, *1*, 398−411.
(46) Egbebi, A.; Schwartz, V.; Overbury, S. H.; Spivey, J. J. Effect of Li promoter on titania-supported Rh catalyst for ethanol formation from CO hydrogenation. *Catal. Today* **2010**, *149*, 91−97.
(47) Luo, L.; Wang, M.; Cui, Y.; Chen, Z.; Wu, J.; Cao, Y.; Luo, J.; Dai, Y.; Li, W. X.; Bao, J.; Zeng, J. Surface iron species in palladium-iron intermetallic nanocrystals that promote and stabilize CO_2 methanation. *Angew. Chem., Int. Ed.* **2020**, *59*, 14434−14442.
(48) Pei, Y.-P.; Liu, J.-X.; Zhao, Y.-H.; Ding, Y.-J.; Liu, T.; Dong, W.-D.; Zhu, H.-J.; Su, H.-Y.; Yan, L.; Li, J.-L.; Li, W.-X. High alcohols synthesis *via* Fischer−Tropsch reaction at cobalt metal/carbide interface. *ACS Catal.* **2015**, *5*, 3620−3624.
(49) Ao, M.; Pham, G. H.; Sunarso, J.; Tade, M. O.; Liu, S. Active centers of catalysts for higher alcohol synthesis from syngas: A review. *ACS Catal.* **2018**, *8*, 7025−7050.
(50) Wang, Y.; Wang, W.; He, R.; Li, M.; Zhang, J.; Cao, F.; Liu, J.; Lin, S.; Gao, X.; Yang, G.; Wang, M.; Xing, T.; Liu, T.; Liu, Q.; Hu, H.; Tsubaki, N.; Wu, M. Carbon-based electron buffer layer on ZnO_x-Fe_5C_2-Fe_3O_4 boosts ethanol synthesis from CO_2 hydrogenation. *Angew. Chem., Int. Ed.* **2023**, *62*, No. e202311786.
(51) Shaw, D. A.; Holland, D. M. P.; Hayes, M. A.; MacDonald, M. A.; Hopkirk, A.; McSweeney, S. M. A study of the absolute photoabsorption, photoionisation and photodissociation cross sections and the photoionisation quantum efficiency of carbon dioxide from the ionisation threshold to 345 Å. *Chem. Phys.* **1995**, *198*, 381−396.
(52) Au, J. W.; Cooper, G.; Brion, C. E. The molecular and dissociative photoionization of ethane, propane, and n-butane: absolute oscillator strengths (10−80 eV) and breakdown pathways. *Chem. Phys.* **1993**, *173*, 241−265.
(53) Kanno, N.; Tonokura, K. Vacuum ultraviolet photoionization mass spectra and cross-sections for volatile organic compounds at 10.5 eV. *Appl. Spectrosc.* **2007**, *61*, 896−902.
(54) Visconti, C. G.; Martinelli, M.; Falbo, L.; Infantes-Molina, A.; Lietti, L.; Forzatti, P.; Iaquaniello, G.; Palo, E.; Picutti, B.; Brignoli, F. CO_2 hydrogenation to lower olefins on a high surface area K-promoted bulk Fe-catalyst. *Appl. Catal., B* **2017**, *200*, 530−542.



https://doi.org/10.1021/jacs.6c02733
J. Am. Chem. Soc. 2026, 148, 19925−19935